Laser ablation of a multilayer target with layers of nanometer thickness

V A Khokhlov[1], S I Ashitkov[2], N A Inogamov[1,3,2], P S Komarov[2], A N Parshikov[3,2], Yu V Petrov[1,4], S A Romashevsky[2], E V Struleva[2], P A Tsygankov[5] and V V Zhakhovsky[3,2]

[1] Landau Institute for Theoretical Physics of the Russian Academy of Sciences, Akademika Semenova 1a, Chernogolovka, Moscow Region 142432, Russia
[2] Joint Institute for High Temperatures of the Russian Academy of Sciences, Izhorskaya 13 Bldg 2, Moscow 125412, Russia
[3] Dukhov Research Institute of Automatics (VNIIA), Sushchevskaya 22, Moscow 127055, Russia
[4] Moscow Institute of Physics and Technology, Institutskiy Pereulok 9, Dolgoprudny, Moscow Region 141701, Russia
[5] Universidad Industrial de Santander, Calle9 # Cra.27, Bucaramanga 680003, Colombia

E-mail: v_a_kh@mail.ru

Abstract. Multilayer products made of ultra-thin layers are widely used in modern science and technology. Laser exposure is used as one of the promising methods of processing such products. In this regard, we study the ablation of a layered target. A physical model is constructed, numerical simulation is performed, and experiments are carried out. The experiments were conducted with two different lasers and various diameters of the focal spot. To estimate the absorbed energy the reflection coefficient was measured. The results of calculations and experiments are consistent with an accuracy of about 10%. This allowed us to refine the model of two-temperature states and determine the strength of nickel. It is explained why, with an increase in the absorbed fluence, first the upper layer breaks in the multilayer.

1. Introduction

Products made from alternating layers of nanometer thickness have many uses. Nickel–aluminum laminates are used as "soft" explosives [1–3]. Multilayer mirrors are the basis of optical systems that control ultraviolet and soft x-rays [4]; such mirrors, for example, are necessary for modern photolithographic machines [4–6]. They process heterostructures—layered structures grown on a substrate from various semiconductors. The laser makes the necessary cuts in the electrodes in alternating thin layers of solar panels (photovoltaicsa; structuring of CIGS thin film solar cells; CIGS—copper indium gallium deselenide) [7,8]. Similar in physical meaning are the problems of selective structuring of single-film targets [8–13].

In this paper, we study a layered target composed of alternating layers of nickel and aluminum. Nickel is the first layer on which the laser beam is incident, figure 1; laser light comes from the left side. In the calculations, the first pair of layers has a thickness of 45 nm, then five pairs of thin layers with a thickness of 25 nm and a thick nickel layer with a thickness of 160 nm instead of a substrate. In the experiment there are more thin layers. The layers are sprayed onto a
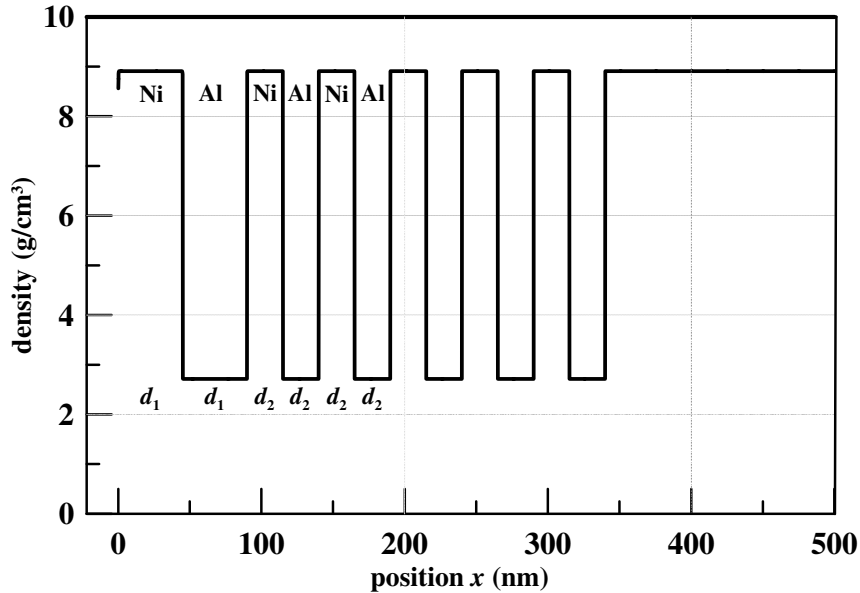
Figure 1. The multilayer scheme—the initional density profile. The first pair of layers of nickel and aluminum are relatively thick ($d_1 = 45$ nm), then 5 pairs of thin layers of Ni and Al ($d_2 = 25$ nm); in the calculation, instead of the substrate, an excess thickness (160 nm) layer of nickel is added; in the experiment, there are more thin layers and a glass substrate.

silicon glass substrate. But in this paper we restrict ourselves to calculating the first threshold. In this case, as will be seen below, only the first few layers of the target play a significant role.

Important information can be obtained from an analysis of the time displacement of the rear side of the target $x_{\text{rear-side}}(t)$. Indeed, the function $x_{\text{rear-side}}(t)$ can be recalculated into the profile shape of the wave traveling to the right (with the orientation of the axis x, taken in figure 1). On this principle is based the analysis of VISAR (Velocity interferometer system for any reflector) [14, 15] and pump-probe experiments (pump-probe, pump-diagnostics [16]) [17–26]. The right-running wave coming out of the multilayer system, should be much wider than in the case of ultrashort shock waves generated by femtosecond pulses in homogeneous volume targets. This is due to internal reflections in the layers. A discussion of this question is beyond the scope of this paper.

We will increase the values of the absorbed fluence F_{abs} from a zero value. In a continuous homogeneous target, there is no visible damage of the target in the laser spot, up to the fluence value $F_{\text{abs}}|_{\text{abl}}$. This value is called the ablation threshold. Significant damage (crater) remains in the target when the value of $F_{\text{abs}}|_{\text{abl}}$ is exceeded. The depth of the crater at the threshold is $x_{\text{crat}}|_{\text{abl}}$. As you can see, the crater is formed by a "jump" when the threshold is exceeded, see, for example, [27–31]. The depth of the crater $x_{\text{crat}}(F_{\text{abs}})$ usually grows monotonously with fluence increasing [27–30, 32, 33].

It is clear that in the case of a multilayer target, there is also an ablation threshold $F_{\text{abs}}|_{\text{abl-1}}$, below which the upper layer (and therefore the lower layers) does not have noticeable damage. However, in the case of a multilayer target, the function $x_{\text{crat}}(F_{\text{abs}})$ when the fluence F_{abs} rises above the first threshold $F_{\text{abs}}|_{\text{abl-1}}$ may have additional jumps [34–36]. These additional jumps are caused by breakes at more and more deeply located contact boundaries. We are talking about contact boundaries between layers of successive different substances. There is a chain of thresholds above the first threshold: $F_{\text{abs}}|_{\text{abl-1}} < F_{\text{abs}}|_{\text{abl-2}} < F_{\text{abs}}|_{\text{abl-3}}, \ldots$ [34–36]. Of course, this behavior is due to the play of reflected and transmitted acoustic waves and the fact that

usually the tensile strength of the contacts is lower than the strength of adjacent homogeneous substances. We will analyze this question below.

It will be seen that due to wave interference, the amplitude of the tensile stress on the contact may be lower than the amplitude of the tensile stresses in the film thickness. For example, when a layer with a finite acoustic impedance Z contacts with two external layers with a low impedance, the tensile stresses on the contacts are small. If the contact strength (contact adhesion) is not too small, then in this situation it is difficult to expect the contact to break.

Note that the question of competition between the internal gap and the gap on the contact of substances was considered in the works [9, 37–40]. In these works, a single layer (film) on the substrate was studied. It has been shown that, depending on the magnitude of contact adhesion and the impedance ratio, two situations are possible. With a not too small ratio of impedances and weak adhesion, the film is detached from the contact at a relatively small value of the absorbed fluence $F_{abs}|_{cb}$ (first scenario); cb is contact boundary; detachment is also called film separation or contact break. Under ultrashort exposure, the contact breaking moment is approximately equal to d_f/c_s [9,37,38], here d_f is the thickness of the film glued to the substrate, c_s is the speed of sound in the film. In this situation, when the fluence F_{abs} increases, a break occurs inside the film at the second threshold $F_{abs}|_{internl}$, $F_{abs}|_{internl} > F_{abs}|_{cb}$ [38–40]. The internal break occurs at a time on the order of $(1/2)d_f/c_s$.

In the second situation, the impedance ratio is small, the strength of contact adhesion is significant. Then there is no delamination of the film from the contact. There is an internal break in the film. Note that the above discussed cases where the impedance of a single film is greater than the impedance of the substrate.

In this paper, we consider the layered target shown in figure 1. Light is absorbed in nickel (1st layer). Because of the finite thickness of the skin layer (δ about 20 nm) and the relatively small thickness of the first nickel layer ($d_1 = 45$ nm), some of the light passes through the nickel film and warms the aluminum layer. But the fraction of transmitted light in comparison with the light absorbed in nickel is small.

The acoustic impedance of nickel significantly exceeds the impedance of aluminum (impedance ratio is about 3). Therefore, as will be shown below, the lowest is the threshold $F_{abs}|_{internal}$, at which the internal break of the first nickel film occurs. Moreover, this threshold is significantly less than the threshold $F_{abs}|_{bulk}$, at which thermomechanical ablation of the bulk nickel target begins. [41–43]. In [41] a free-hanging film of finite (50 nm) thickness is considered, so that it does not give a breakdown threshold for a continuous target. According to [43, equations (1.2), (1.3)] at threshold $F_{abs} \approx 140$ mJ/cm^2, $d_{crat} \approx 20$ nm. The fact is that in the case of a sufficiently thin film, there are two rarefaction waves running from the front and back boundaries of the film [9, 42]. Summing up, they increase the tensile stress. This addition lowers the threshold for the absorbed fluence in comparison with the case of a bulk target, when the rarefaction wave is one—running from the frontal boundary. Above in this paragraph, the words "sufficiently thin film" mean that the thickness of the film is not too much greater than the thickness of the laser heating layer d_T.

2. Experiment

The experiments carried out have a number of features that are very important for understanding the essence of the matter. To quantitatively compare the results of experiments and calculations, it is necessary to know the amount of energy absorbed by the target (fluence F_{abs}) during a single exposure session. It is not easy to determine this value. In ordinary experimental descriptions, the incident fluence is given F_{inc}. But in metals in the optical radiation range, the reflection coefficient $R(\omega)$ is significant. Therefore, only part of the incident radiation $F_{abs} = (1 - R)F_{inc}$ works in the target.

The Fresnel formulas and the constant reference value of the complex refractive index $n(\omega)$

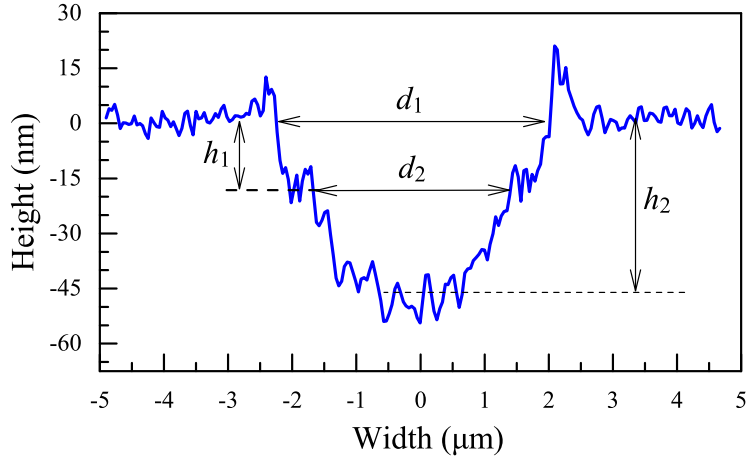**Figure 2.** Profile of the crater at the sample surface measured by AFM. Laser fluence in center of spot is above the second threshold $F_{\mathrm{abs}}|_0 > F_{\mathrm{abs}}|_{\mathrm{abl}\text{-}2}$. Diameters d_1 and d_2 of the craters at the first and second spallation, respectively, are used to calculate the threshold fluence, h_1 and h_2 are the corresponding crater depths.

cannot be used to calculate the coefficient $R(n)$. The fact is that under femtosecond exposure, complex refractive index $n(t)$, $n = \sqrt{\varepsilon}$, ε is the dielectric constant, changes during the pulse. As known, this is due to the strong excitation of the electronic subsystem. There are theoretical calculations of the indicator $n(t)$. But they are based on a physical model of two-temperature states. Meanwhile, this model itself needs to be tested in experiments. The change in the refractive index n due to the transition to the two-temperature state is especially significant for well-reflecting metals. In our case, the reflection coefficient of nickel is not large. And the effect of the change in the n indicator is quite small.

It is very important that in our experiments the amount of absorbed energy was determined directly during the experiment. The description of the details of the experiments requires a separate statement consideration. Accordingly, in numerical simulation, we operated with precisely measured absorbed energy F_{abs}; as mentioned, this is important for comparing calculations and experiments.

Another important condition is the following. Experiments were conducted in parallel on two different femtosecond lasers with different diameters of the focus spot. This seems to be the first time this approach has been applied in the class of problems under consideration. The ytterbium fiber laser had a sharp focus close to the diffraction limit; the pulse duration was 350 fs. On the other system, the usual big-spot focus was applied. The TiS system was used. The beam fell at an angle of 60 degrees from the normal; p-polarization, pulse duration 40 fs. The semiaxes of the ellipse of the illumination spot were 22 and 45 μm at a level of $1/e$.

Impacts with a small spot were applied earlier [44–46, and citations there]. Large spot exposures are common [20, 47]. In this paper, as mentioned, probably for the first time, both approaches are used together. Such a comparison greatly improves the reliability of the data obtained. The threshold value on incident fluence was determined from dependence of diameter of the crater on pulse energy [48]. The diameter d and depth h of craters were measured by atomic force microscopy (AFM) or interferometric technique with a nanometric accuracy. As an example figure 2 shows the profile of a crater measured using AFM.

Here are the main data obtained in such, firstly, joint experiments, and secondly, with the determination of the reflection coefficient. With this data, we will compare the results

of numerical modeling. The first ablation threshold is

$$F_{\text{abs}}|_{\text{abl-1}} \approx 40 \text{ mJ/cm}^2 \qquad (1)$$

for absorbed fluence. It is important that the first spallation occurs not at the first nickel–aluminum contact, but in the thickness of the first nickel layer, see figures 1 and 2. The depth of the crater on the threshold is

$$x_{\text{crat}}|_{\text{abl-1}} \approx 20\text{–}25 \text{ nm}, \qquad (2)$$

which is close to half the layer thickness.

The second spallation occurs at the boundary of the first contact between nickel and aluminum. The threshold energy of the second spall is

$$F_{\text{abs}}|_{\text{abl-2}} = 160\text{–}200 \text{ mJ/cm}^2. \qquad (3)$$

As you can see, for the second spall, a large 4–5-fold excess in energy is required, see (1), (3). The crater depth at the second threshold is

$$x_{\text{crat}}|_{\text{abl-2}} \approx 45 \text{ nm}. \qquad (4)$$

Note also that according to the data obtained from our experiments, the ablation threshold of a homogeneous bulk thick target made of nickel is

$$F_{\text{abs}}|_{\text{abl}} = 160 \text{ mJ/cm}^2; \qquad x_{\text{crat}}|_{\text{abl}} = 20 \text{ nm}. \qquad (5)$$

3. Physical model and calculation scheme

Large literature is devoted to the description of the physics of two-temperature states, which continues to be replenished. The expansion of the literature is connected with the problems of research of such states. Our model is based on the separation of electronic and ionic contributions to free energy. [13,49–52] The split-contribution approach goes back to the work of the 60s. Then it became necessary to describe hot media with a density on the order of solid-state density. But these were hot, dense, one-temperature states; one-temperature, mean the temperatures of the electron and ion subsystems are equal. A new situation arose when fast laser heating led to a sharp excess of the electron temperature over the ion temperature.

In the first work [49], and in many papers so far, the authors have limited themselves to the thermophysics of the electron and ion subsystems. But this is not enough to describe phenomena near and above the ablation threshold F_{abl}. With this energy of laser action, hydrodynamic processes begin to play a significant role: displacement, compression and stretching of the substance.

In our calculations (results below) we use the previously developed two-temperature (2T) hydrodynamic code 2T-HD [50, 51] see also [33, 53, 54]. The consideration of multilayering is reduced to the fact that in the interval of Lagrangian cells related to each material, the equations of state, electron–ion heat transfer and thermal conductivity for this material are used. The Lagrangian grid is chosen so that the boundaries of different substances fall on the grid nodes. Since the Lagrangian coordinate is attached to the substance, the initial reference of cells and substances is preserved.

Mechanical boundary conditions at the boundaries of different substances are performed automatically. The boundary conditions in the thermal problem are not so trivial. The thickness of the first layer of nickel $d_1 = 45$ nm (see figure 1) is more than twice the thickness of the skin layer $\delta = 20$ nm, so the main part of the laser radiation is absorbed in this layer. This allow us to neglect the possible effects of reflection at the interface between nickel and aluminum and assume that the heat release power obeys the Bouguer law with a constant decay length δ (the thickness of the skin layer in intensity). As will be seen later, heating due to thermal conductivity is not very significant in comparison with the action of the compression wave, coming out of the first

hot layer. Therefore, we neglect all possible thermal effects on the border of the two metals, and believe that there remains the electron temperature and heat flux. Then it is enough to assume that the thermal conductivity coefficient at the boundary of metals 1 and 2

$$\kappa_{1-2} = \frac{\kappa_1 \kappa_2 (x_{b+1} - x_{b-1})}{\kappa_1 (x_{b+1} - x_b) + \kappa_2 (x_b - x_{b-1})},$$

where κ_1, κ_2 are thermal conductivity coefficients for metal 1 and 2, respectively, x_b, x_{b-1}, x_{b+1} are coordinates of the border (Lagrangian node on the border), the preceding Lagrangian node (in metal 1) and the next Lagrangian node (in metal 2).

Although it is referred to as "hydrodynamics", the code describes in a cross-cutting manner both hydrodynamics and the mechanics of a deformable solid (MDTT). Solid mechanics is described both in the plastic approximation and with the use of elastoplastics models [23–25, 55]. Below, it will be enough for us to limit ourselves to a plastic approximation. An end-to-end description of the solid and liquid phases is necessary in the analysis of laser exposure problems because there are processes of melting and crystallization.

4. Early stage, first picosecond, abnormal temperature profiles

In this paper, we will limit ourselves to calculating first threshold for the absorbed energy $F_{abs}|_{abl-1}$ and determining the depth of the crater $x_{crat}|_{abl-1}$ at first threshold. This will allow us to verify the model used by comparing with the experimental data (1) and (2). As will be seen below, the calculations are consistent with the experiments. Therefore, the model adequately describes the physics of the processes. In the future, using this proven approach, numerical simulations will be performed to determine second threshold $F_{abs}|_{abl-2}$ (3). Hopefully, it will be possible to determine the strength of adhesion on the contact between the sprayed nickel and aluminum, see figure 1, where this contact is shown. Next, calculations will be performed for comparison with experiments in statement (5).

First spall occurs on the sound time scales $t_s = d_f/c_s$. Substituting here the sound velocity in nickel of 4.6 km/s and the thickness of first film 45 nm (see figure 1), we find $t_s \approx 10$ ps. At such times, only 2 maximum 3 first layers of the multilayer target interact hydrodynamically.

The presentation of the results naturally begins with the early stages and the thermal picture. The fact is that with femtosecond exposure, the initial propagation of heat from the skin layer occurs at supersonic speed [55, 56]. A little later, the hydrodynamic effects associated with the propagation of acoustic waves with the speed of sound become significant.

Let us compare the material characteristics that are essential for describing the ultrashort effect on nickel and aluminum nanometer films. First, there is an impressive difference in the electronic heat capacity $C_e(T_e, \rho)$. Under normal conditions, the heat capacity C_e of nickel is an order of magnitude greater. This is due to structure of the electronic spectrum of nickel $3d^{8-9} 4s^{2-1}$ compared to aluminum $3s^2 3p^1$. Nickel has a much denser spectrum of electronic states below and above the Fermi level compared to aluminum. Due to the difference in heat capacity C_e, the electron temperature T_e of nickel is lower than in aluminum, with equal electron energy densities per unit volume.

Secondly, the ionic heat capacity of nickel per unit volume is 1.5 times higher than that of aluminum. If thermal conductivity processes are not taken into account, this circumstance is the reason for higher ion temperatures T_i in aluminum at equal ionic energy densities per unit volume. Finally, thirdly, nickel is significantly stiffer than fairly soft aluminum. As mentioned above, the acoustic impedance of nickel is three times greater.

We see that the usual course of temperature T_e deep into the target is broken. An anomaly in the electron temperature profiles at an early stage is associated with the difference in heat capacities C_e noted above. Let us look at figure 3. Namely, there is an inverse section where the electron heat does not flow into the depth of the target, but in the opposite direction—towards
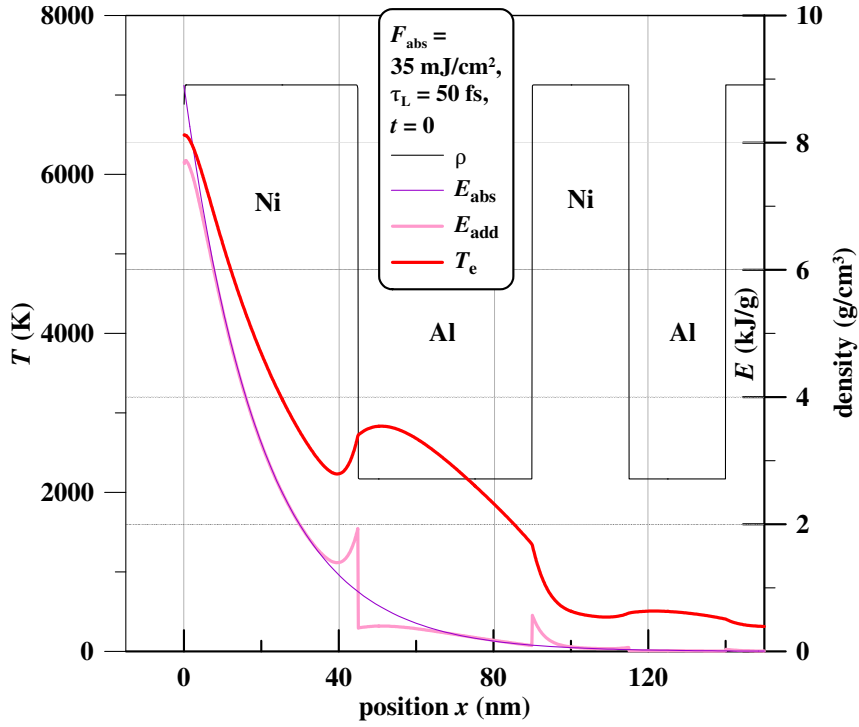
Figure 3. Absorbed (E_{abs}) and additional (E_{add}) electron energy and electron temperature T_{e}.
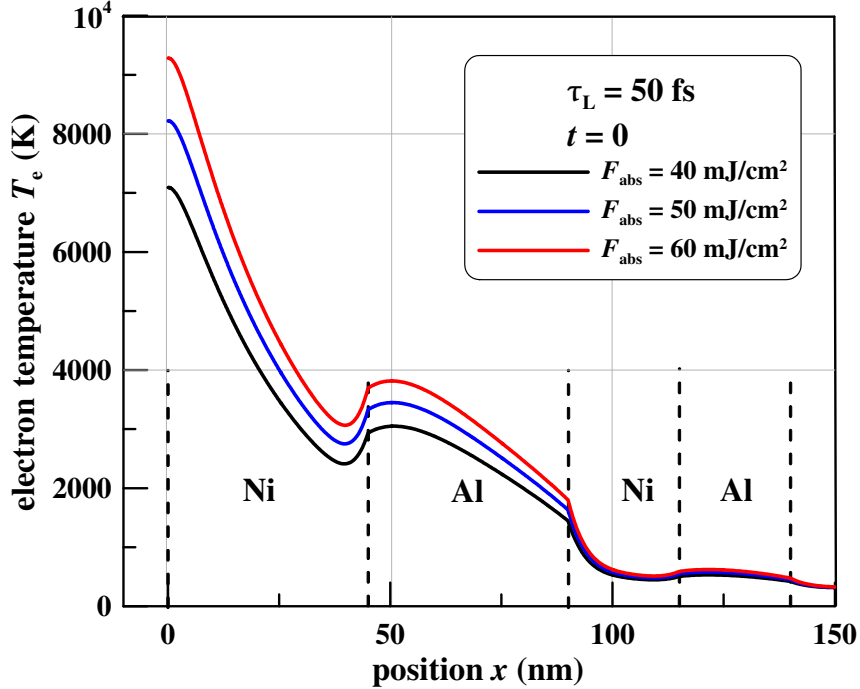

Figure 4. Electron temperature profiles at different absorbed energy.

the front (that is, irradiated) surface! This anomaly also leads to an anomaly in the profile of energy, added to the electronic subsystem E_{add}, see figure 3. At the early stage considered here, this energy is formed mainly due to the absorption of laser radiation (absorbed energy E_{abs}),
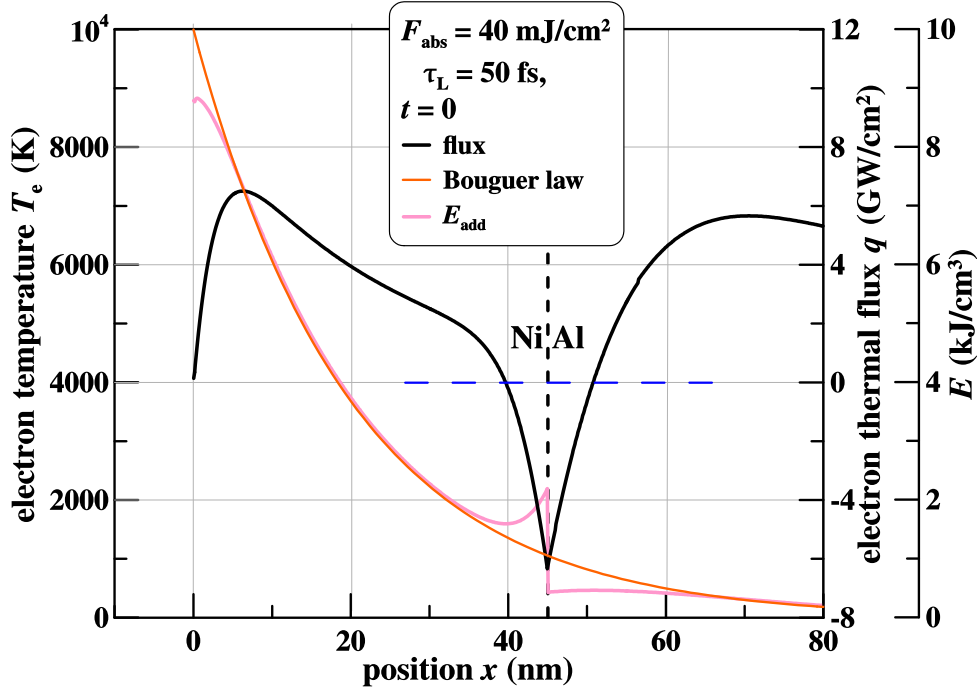
Figure 5. Electron temperature profile T_{e}, electron heat flux q heat release power and increase in electron energy E_{add}.

but is partially redistributed by thermal conductivity. Then, during the 2T stage, the main effects become the flow of energy from the heated region deep into the target due to thermal conductivity and the transfer of energy from the electronic subsystem to the ionic one, and effects associated with the movement of matter undoubtedly dominate in the acoustic stage. Figure 4 shows the results of a series of calculations corresponding to the time $t = 0$ for different absorbed fluences F_{abs}. The situation with the anomaly is the same. The time in our calculations is calculated from the maximum intensity of the laser pulse $I(t) \propto \exp(-t^2/\tau_{\mathrm{L}}^2)$. The full width of the pulse at level $1/e$ is equal to $2\tau_{\mathrm{L}} = 100$ fs. By the time $t = 0$, half of the total absorbed fluence F_{abs}, specified in the captions under each of the graphs 3 and 4, has been entered into the target.

In figure 5 instantaneous electron temperature profiles T_{e}, electron heat flux q heat release power ε [W/m^3] per unit volume according to Bouguer's law $\varepsilon \propto \exp(-x/\delta)$ with a decay length of $\delta = 20$ nm (the thickness of the skin layer in intensity) and increase in electron energy E_{add}. The Bouguer distribution $\varepsilon \propto \exp(-x/\delta)$ in figure 5 is given in dimensionless units. For heat generation ε a simplified Bouguer law was adopted, in which we did not take into account the refraction of light at the contact boundary between nickel and aluminum. This approach is justified, since a small amount of laser energy reaches the contact.

Thus, the difference in the heat capacities C_{e} in nickel and aluminum with a continuous heat output ε at the contact leads to the inversion of the electron heat flux and the anomaly in the electron temperature profile in figure 5. In figure 5 the horizontal line indicates the zero heat flux, and the vertical line indicates the contact position between nickel and aluminum. Note that the electronic heat flow is units of GW/cm^2. At the same time, the absorbed intensity of the light flux $I_{\mathrm{abs}} \sim F_{\mathrm{abs}}/\tau_{\mathrm{L}}$ is two orders of magnitude higher—hundreds of GW/cm^2. That is, the energy in the skin layer of the film arrives per unit time two orders of magnitude more than is diverted due to electronic thermal conductivity. Therefore, firstly, the electronic temperature increases
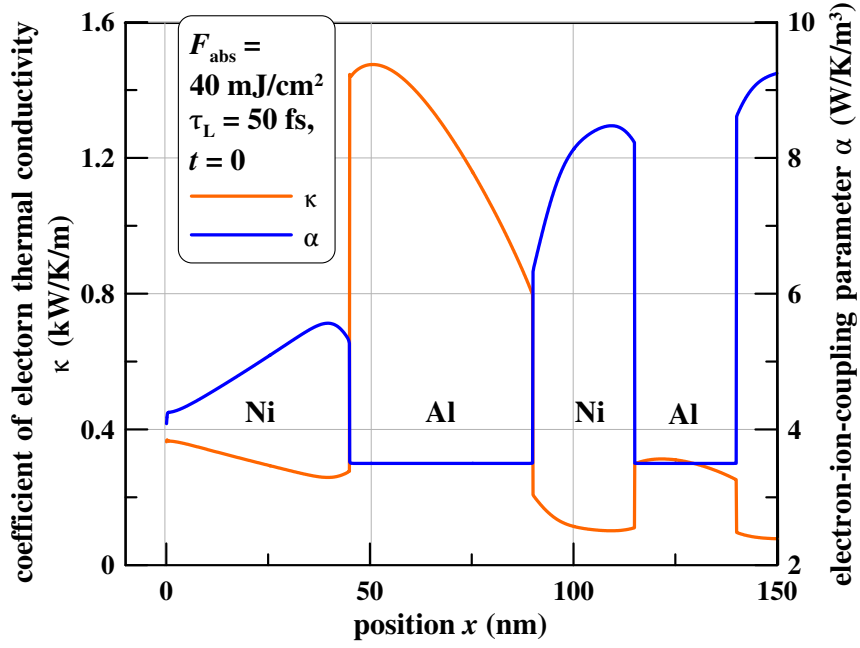
Figure 6. Coefficients of electronic thermal conductivity κ and of electron-ion interaction α.
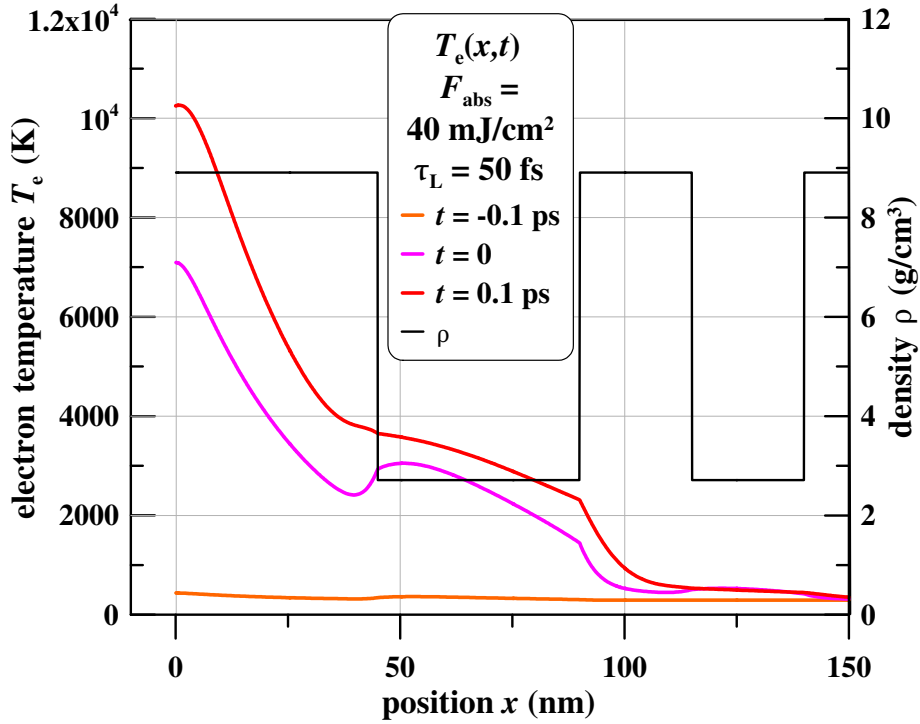

Figure 7. Evolution of electron temperature T_e profiles.

during the pulse and, secondly, the heat sink from the skin continues for a considerable time after the end of the pulse. To complete the picture figure 6 shows the profiles of the coefficient of electronic thermal conductivity κ and the coefficient of electron–ion interaction α.

However, the abnormal behavior shown in figures 3–5 does not last long. This is due to
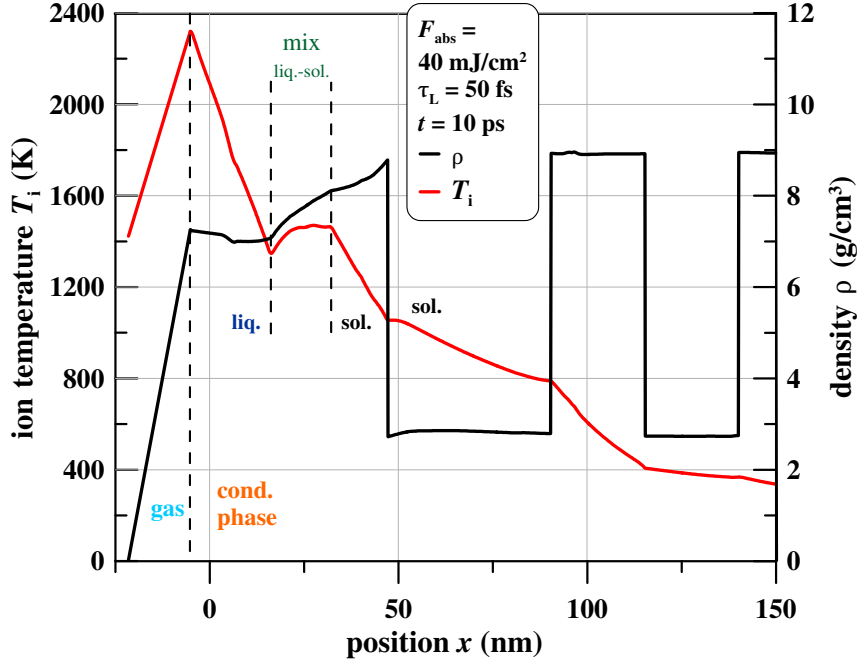
Figure 8. Phase states of layers.

the small amount of light energy that enters aluminum through the nickel film. By the first picosecond after the ultrashort laser pulse, the profiles of the electron temperature and the electron energy flow assume the usual monotonous form. The evolution of instantaneous profiles from the anomalous to the normal type is shown in figure 7.

A quick return to the standard form is due to the following circumstance. The energy accumulated in the skin layer during a pulse with an intensity of hundreds of GW/cm^2, is then removed with a heat flux of the order of GW/cm^2 to the thickness of the films. Thus a small amount of energy penetrated into the aluminum for the pulse time is irrelevant. Indeed, this amount is small compared with the energy accumulated in the skin layer. The accumulated energy is relatively long (compared with the duration of τ_L) removed from the skin layer. The cooling of the skin layer takes a relatively long time due to the relatively low intensity of the electron heat flux.

5. Energy transfer to the ionic subsystem and melting

The determining hydrodynamic motion begins at the acoustic stage, at times starting from a few picoseconds. But before we begin to describe the force fields and the reaction of matter (compression, stretching), let us talk about the change in the phase state due to heating. This is important for understanding thebreaking process in a substance (thermomechanical ablation process), since the tensile strength of a substance is significantly reduced by melting. Figure 8 shows a typical alternation of layers of different phases at the stage when the transfer of energy from the electronic subsystem to the ion subsystem is almost complete. This means that the two-temperature stage is almost complete and the substances are in one-temperature states.

The alternation of the layers vapor–liquid phase–two-phase mixture–solid phase is shown in figures 8 and 9. A two-phase mixture consists of liquid and solid phases. The melting threshold is a rather poorly defined value. If we take the absorbed fluence F_{abs}, at which a pure liquid phase appears near the border with air, then this threshold is somewhere in the fluence range F_{abs} from 35 to 40 mJ/cm^2, see figure 9. If the threshold is taken as a fluence, at which a mixture
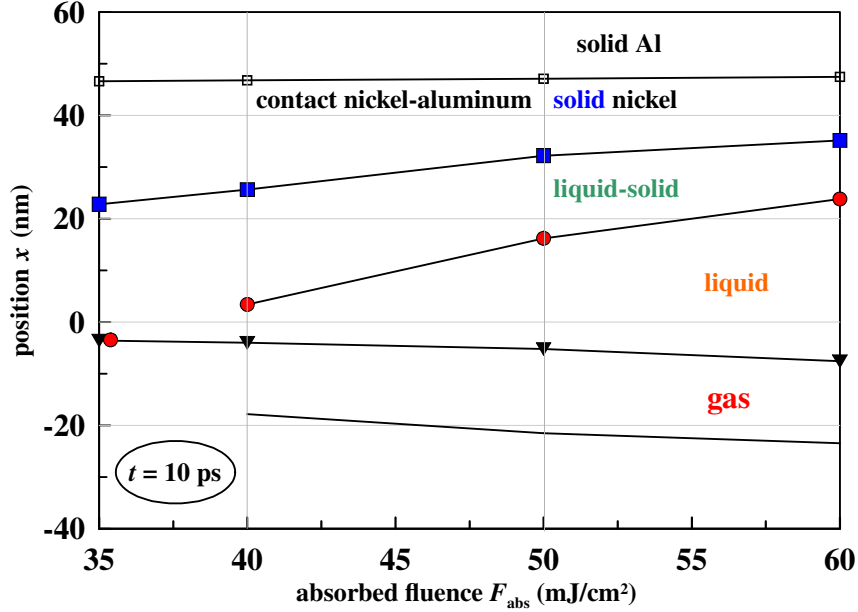
Figure 9. Phase boundaries.

of melt and crystal is formed at the border, then the threshold fluence will be significantly less.

At the time $t = 10$ ps, shown in figures 8 and 9, an acoustic wave propagates through the first layers of nickel and aluminum. In this wave, the contact and the aluminum near the contact are under compressive pressure, see text below. Meanwhile, the region of the two-phase mixture of liquid and solid nickel is stretched under negative pressure. The melting point T_m is a function of the pressure $T_\mathrm{m}(p)$. Therefore, nickel melts at a temperature below the temperature $T_\mathrm{m}(p = 0) = 1728$ K. While aluminum near the contact boundary remains in the crystalline state, although its temperature is higher than the melting point of aluminum $T_\mathrm{m}(p = 0) = 934$ K under negligible pressure of aluminum vapors at this temperature.

6. Acoustic stage, pressure profiles

A typical pressure profile is shown in figure 10. This is the profile at the stage where the first nickel film is subjected to strong tension. Stretching is associated with the summation of rarefaction waves coming from the boundary with air and from the boundary with aluminum. In these rarefaction waves, the first nickel layer is unloaded towards acoustically weaker media. Unloading at acoustic times is caused by a rise in pressure in the first nickel layer due to rapid laser heating.

In figure 10 a red vertical straight line and a red circlemarker point out the position of the place of greatest tension at time 15 ps. Figure 11 shows how the amplitude of the highest tensile stress $|P_{xx}|_\mathrm{max}$ changes over time. Cases with values of the absorbed fluence equal to 40 and 60 mJ/cm^2 are considered. We see that due to the saturation of the dependence $p(\rho)$, the amplitude $|P_{xx}|_\mathrm{max}$ changes little when the fluence F_abs increases by a factor of 1.5 from the value of 40 mJ/cm^2. Under the dependence $p(\rho)$ here we assume the dependence of cold pressure on density. This dependence begins to saturate when approaching the minimum.

Another significant circumstance is the following. The tensile stress is kept for a long time (5–7 ps) near its highest value ("plateau"), see figure 11. This increases by several times the value of the preexponential factor in the expression for the probability of nucleation of the bubble in the expanded nickel melt.

Figure 12 shows the longitudinal velocity profile in the vicinity of the segment along the x
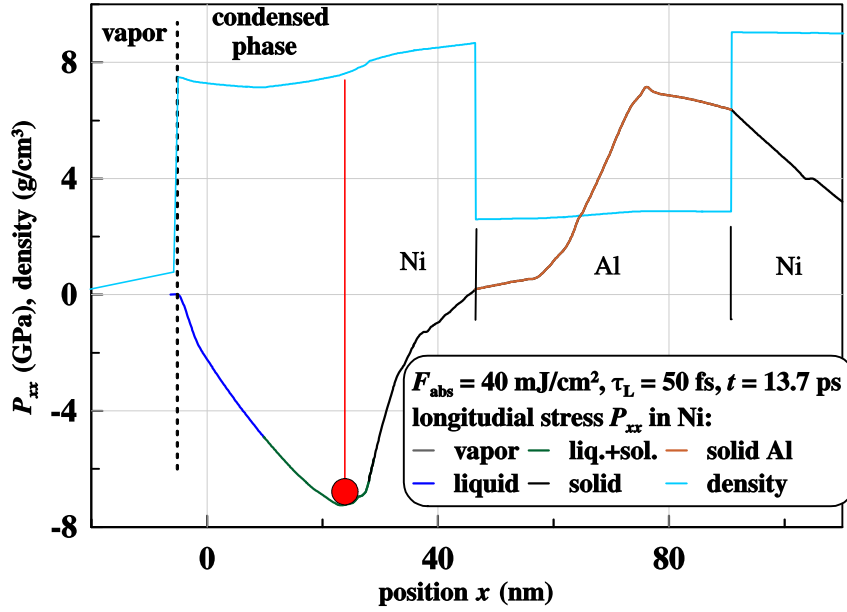
Figure 10. Pressure profile before break point. Red vertical straight line and a red circlemarker point out the position of the place of greatest tension.
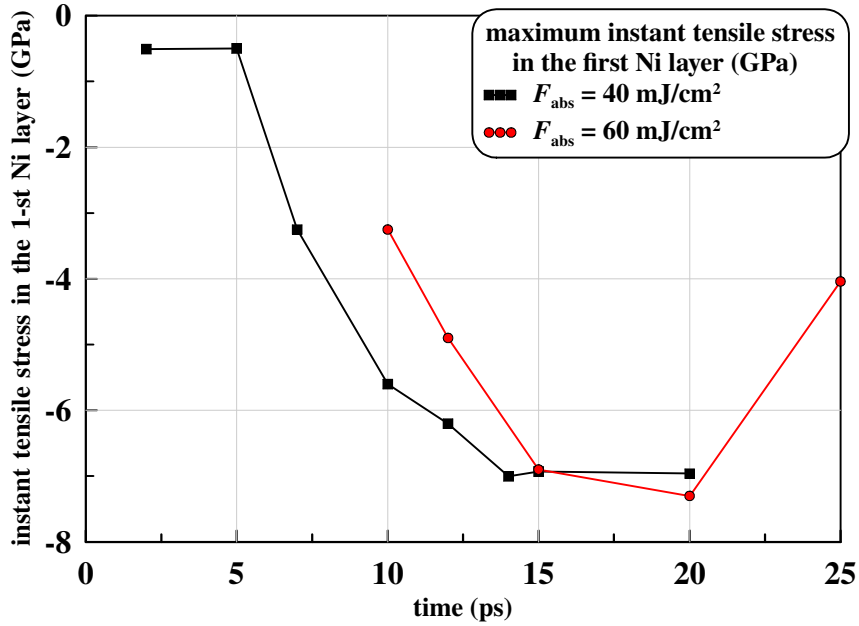

Figure 11. Change in the highest shear stress $|P_{xx}|_{\max}$ over time.

axis, on which the greatest stretchings are achieved, shown in figures 10 and 11. Let us estimate the stretching rate $\dot{V}/V$ according to figure 12.

We have:

$$\dot{V}/V = (d(\Delta x)/dt)/\Delta x = \Delta u/\Delta x = 3 \times 10^9 \ 1/\text{s}. \tag{6}$$

For Δx in (6), we took the length of the segment along the x axis, shown in figure 12. Herewith the speed difference Δu at the ends of this segment is approximately 8 m/s.
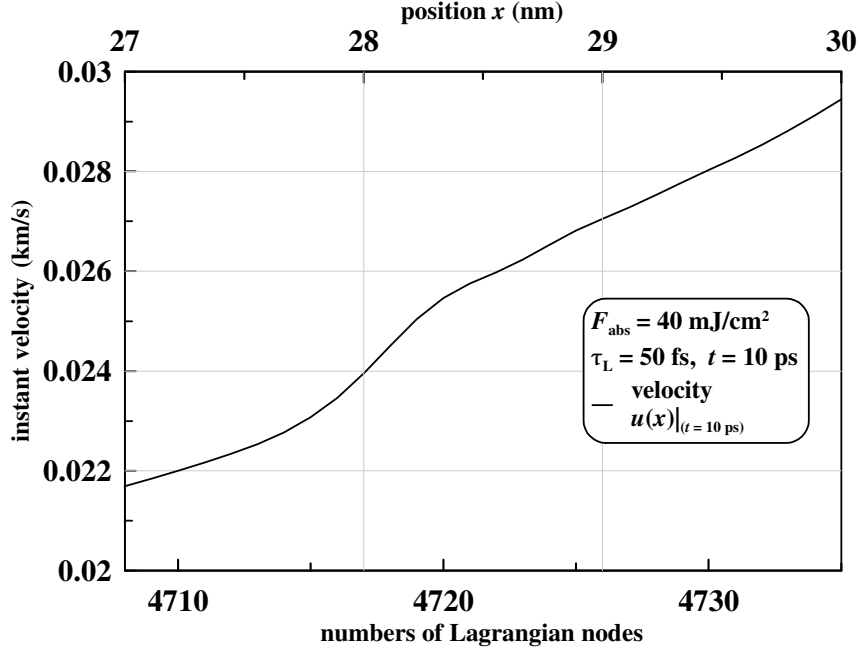
Figure 12. Velocity profile in the segment along the x axis, on which the greatest stretchings are achieved.

Take the data on the strength of the melt of nickel from the article [57]. According to this work, the strength of the liquid phase σ decreases with increasing temperature approximately according to the law

$$\sigma = s_0 - s_1 T, \tag{7}$$

where $s_0 = 11.4$ GPa, $s_1 = 2.2$ GPa/kK, T in kK. The expression (7) is obtained according to the article [57], if we assume that the stretching rate is three times lower than the value (6). We consider this decrease in the rate of stretching to be justified, since nickel in the stretching zone has been in a stretched state for quite some time, see figure 11. Near the melting point of Nickel at zero pressure $T_m(p = 0) = 1728$ K formula (7) gives a strength value of σ at $T = 1.728$ kK approximately 7.6 GPa. For more accurate strength calculation, additional molecular dynamics calculations are required. According to our simulation, nickel in the layer of greatest tension is either in the liquid phase or in the state of a two-phase mixture, see figures 8 and 9.

7. Breaking criterion and ablation threshold

From what was said in the previous section, it follows that there is an uncertainty of the order of 10% relative to at what tensile stress nucleation inside the nickel will begin. Our calculated data, taking into account such an error, indicate the following:

- First, the first break occurs in the first layer of nickel, not on the first nickel–aluminum contact.
  Words "first break" refer to the spall threshold at the smallest fluence value $F_{abs}|_{abl-1}$ with the growth of fluence F_{abs} from zero.
- Second, the threshold value $F_{abs}|_{abl-1}$ is about 40 mJ/cm^2. This value is in good agreement with experiment (1).
- Third, the depth of the gap $x_{craft}|_{abl-1}$ is 20–30 nm, which also agrees well with the experiments (2).

Additionally note. The depth of the internal break in nickel varies little with the fluence (see figure 11). The pressure at the first contact boundary remains positive in the considered time range up to about 20 ps.

8. Conclusions

An extensive cycle of experimental measurements was performed on two laser systems. The measurements were carried out on a layered target of alternating layers of nickel and aluminum. The advantages of our measurements are that there were two lasers. They differed greatly. The radiation was focused into a small (ytterbium system) and a large (TiS laser) spot of illumination. Thresholds and crater depths were compared. This greatly increased the reliability of experimental data.

It is very important that each experiment quantified how much energy F_{abs} absorbed by the target. Just on this circumstance a detailed comparison of the data of experiments and calculations is based.

The calculations allowed us to look "inside" what is happening in the films. An inverse behavior of the electron temperature profile at an early stage was found, see section 4. The melting process is analyzed as energy is transferred from the electron subsystem to the ion subsystem, see section 5. The interference of acoustic waves inside the first nickel layer was studied, see section 6. Finally, the analysis of tensile stresses and the rate of deformation allowed us to draw theoretical conclusions about the amplitude of $F_{abs}|_{abl-1}$ and the crater depth $x_{crat}|_{abl-1}$, section 7. It turned out that the theoretical values are in good agreement with the experiments, compare sections 2 and 7.

References

[1] Benson D J and Nesterenko V F 2001 *J. Appl. Phys.* **89** 3622
[2] Mann A B, Gavens A J, Reiss M E, Van Heerden D, Bao G and Weihs T P 1997 *J. Appl.Phys.* **82** 1178–88
[3] Weingarten N S and Rice B M 2011 *J. Phys.: Condens. Matter* **23** 275701
[4] Barysheva M M, Pestov A E, Salashchenko N N, Toropov M N and Chkhalo N I 2012 *Phys. Usp.* **55** 681–99
[5] Grigoryev S Yu *et al* 2018 *Phys. Rev. Applied* **10** 064009
[6] Abramenko D B *et al* 2019 *Phys. Usp.* **62** 304–14
[7] Bovatsek J, Tamhankar A, Patel R S, Bulgakova N M and Bonse J 2010 *Thin Solid Films* **518** 2897–904
[8] Domke M, Nobile L, Rapp S, Eiselen S, Sotrop J, Huber H P and Schmidt M 2014 *Phys. Procedia* **56** 1007–14
[9] Inogamov N A, Zhakhovskii V V and Khokhlov V A 2015 *J. Exp. Theor. Phys.* **120** 15–48
[10] Inogamov N A, Zhakhovsky V V, Khokhlov V A, Petrov Yu V and Migdal K P 2016 *Nanoscale Res. Lett.* **11** 177
[11] Kuchmizhak A *et al* 2016 *Nanoscale* **8** 12352–61
[12] Pflug T, Wang J, Olbrich M, Frank M and Horn A 2018 *Appl. Phys. A* **124** 116
[13] Khokhlov V A, Petrov Y V, Inogamov N A, Migdal K P, Winter J, Aichele C, Rapp S and Huber H P 2019 *J. Phys.: Conf. Ser.* **1147** 012066 (arXiv:1811.10312 [cond-mat.mes-hall])
[14] Antoun T, Seaman L, Curran D R, Kanel G I, Razorenov S V and Utkin A V 2003 *Spall Fracture (Shock Wave and High Pressure Phenomena)* (Springer)
[15] Kanel' G I, Fortov V E and Razorenov S V 2007 *Phys. Usp.* **50** 771–91
[16] Temnov V V, Sokolowski-Tinten K, Zhou P and von der Linde D 2006 *J. Opt. Soc. Am.* B **23** 1954–64
[17] Evans R *et al* 1996 *Phys. Rev. Lett.* **77** 3359–62
[18] Gahagan K T, Moore D S, Funk D J, Rabie R L, Buelow S J and W N J 2000 *Phys. Rev. Lett.* **85** 3205–8
[19] Moore D S, Gahagan K T, Reho J H, Funk D J, Buelow S J, Rabie R L and Lippert T 2001 *Appl. Phys. Lett.* **78** 40–2 (*Preprint* https://doi.org/10.1063/1.1337629)
[20] Funk D, Moore D, Mcgrane S, Gahagan K T, Reho J H, Buelow S J, Nicholson J, Fisher G L and Rabie R 2004 *Thin Solid Films* **453–454** 542–9

[21] Agranat M B, Anisimov S I, Ashitkov S I, Zhakhovskii V V, Inogamov N A, Komarov P S, Ovchinnikov A V, Fortov V E, Khokhlov V A and Shepelev V V 2010 *JETP Lett.* **91** 471–7
[22] Ashitkov S I, Agranat M B, Kanel' G I, Komarov P S and Fortov V E 2010 *JETP Lett.* **92** 516–20
[23] Zhakhovskii V V and Inogamov N A 2010 *JETP Lett.* **92** 521–6
[24] Inogamov N A, Zhakhovskii V V, Khokhlov V A and Shepelev V V 2011 *JETP Lett.* **93** 226–32
[25] Zhakhovsky V V, Budzevich M M, Inogamov N A, Oleynik I I and White C T 2011 *Phys. Rev. Lett.* **107** 135502
[26] Ashitkov S I, Komarov P S, Agranat M B, Kanel G I and Fortov V E 2013 *JETP Lett.* **98** 384–8
[27] Anisimov S I, Zhakhovskii V V, Inogamov N A, Nishihara K, Petrov Yu V and Khokhlov V A 2006 *J. Exp. Theor. Phys.* **103** 183–97
[28] Agranat M B, Anisimov S I, Ashitkov S I, Zhakhovskii V V, Inogamov N A, Nishihara K, Petrov Yu V, Fortov V E and Khokhlov V A 2007 *Appl. Surf. Sci.* **253** 6276–82
[29] Inogamov N A, Zhakhovskii V V, Ashitkov S I, Petrov Yu V, Agranat M B, Anisimov S I, Nishihara K and Fortov V E 2008 *J. Exp. Theor. Phys.* **107** 1–19
[30] Zhigilei L V, Lin Z and Ivanov D S 2009 *J. Phys. Chem.* C **113** 11892–906
[31] Loktionov E Y, Ovchinnikov A V, Protasov Y S, Protasov Yu Yu and Sitnikov D S 2012 *Opt. Spectrosc.* **112** 631
[32] Povarnitsyn M E, Itina T E, Sentis M, Khishchenko K V and Levashov P R 2007 *Phys. Rev.* B **75** 235414
[33] Povarnitsyn M E, Fokin V B and Levashov P R 2015 *Appl. Surf. Sci.* **357** 1150–6
[34] Gaković B, Tsibidis G D, Skoulas E, Petrović S M, Vasić B and Stratakis E 2017 *J. Appl. Phys.* **122** 223106
[35] Romashevskiy S A, Tsygankov P A, Ashitkov S I and Agranat M B 2018 *Appl. Phys.* A **124** 376
[36] Kudryashov S I, Gakovic B, Danilov P A, Petrovic S M, Milovanovic D, Rudenko A A and Ionin A A 2018 *Appl. Phys. Lett.* **112** 023103
[37] Inogamov N A and Zhakhovskii V V 2014 *JETP Lett.* **100** 4–10
[38] Khokhlov V A, Inogamov N A, Zhakhovsky V V, Shepelev V V and Il'nitsky D K 2015 *J. Phys.: Conf. Ser.* **653** 012003
[39] Khokhlov V A, Zhakhovsky V V, Khishchenko K V, Inogamov N A and Anisimov S I 2016 *J. Phys.: Conf. Ser.* **774** 012100
[40] Khokhlov V A, Inogamov N A, Zhakhovsky V V, Ilnitsky D K, Migdal K P and Shepelev V V 2017 *AIP Conf. proc.* **1793** 100038
[41] Ivanov D S and Zhigilei L V 2003 *Phys. Rev.* B **68** 064114
[42] Demaske B J, Zhakhovsky V V, Inogamov N A and Oleynik I I 2010 *Phys. Rev.* B **82** 064113
[43] Inogamov N A *et al* 2012 *AIP Conf. Proc.* **1464** 593–608
[44] Romashevskiy S A, Ashitkov S I and Agranat M B 2016 *Appl. Phys. Lett.* **109** 261601
[45] Romashevskiy S A, Ashitkov S I, Ovchinnikov A V, Kondratenko P S and Agranat M B 2016 *Appl. Surf. Sci.* **374** 12–8
[46] Wang X W *et al* 2017 *Phys. Rev. Appl.* **8** 044016
[47] Struleva E V, Komarov P S and Ashitkov S I 2019 *High Temp.* **57** 659–62
[48] Liu J M 1982 *Opt. Lett.* **7** 196–8
[49] Anisimov S I, Kapeliovich B L and Perel'man T L 1974 *Sov. Phys. JETP* **39** 375–7
[50] Anisimov S I, Inogamov N A, Petrov Yu V, Khokhlov V A, Zhakhovskii V V, Nishihara K, Agranat M B, Ashitkov S I and Komarov P S 2008 *Appl. Phys. A* . A **92** 939–43
[51] Inogamov N A, Zhakhovskii V V and Khokhlov V A 2018 *J. Exp. Theor. Phys.* **127(1)** 79–106
[52] Khokhlov V A, Zhakhovsky V V, Petrov Yu V, Shepelev V V, Ilnitsky D K, Migdal K P and Inogamov N A 2019 *J. Phys.: Conf. Ser.* **1147** 012070
[53] Povarnitsyn M E, Itina T E, Sentis M, Khishchenko K V and Levashov P R 2007 *Phys. Rev.* B **75** 235414
[54] Povarnitsyn M E, Itina T E, Levashov P R and Khishchenko K V 2013 *Phys. Chem. Chem. Phys.* **15** 3108–14
[55] Khokhlov V A, Inogamov N A, Anisimov S I, Zhakhovsky V V, Shepelev V V, Ashitkov S I, Komarov P S, Agranat M B and Fortov V E 2010 Investigation of two-temperature relaxation in thin foil on a glass substrate initiated by the action of ultrashort laser pulse *Equations of States of Matter — 2010, The compendium of the XXV Int. Conf. on Equations of State for Matter, Ed. by Fortov V.E. et al., March 1-6, 2010, Elbrus, Kabardino-Balkaria, Russia.* (Chernogolovka) pp 127–9
[56] Inogamov N A, Zhakhovsky V V, Ashitkov S I, Khokhlov V A, Shepelev V V, Komarov P S, Ovchinnikov A V, Sitnikov D S, Petrov Yu V, Agranat M B, Anisimov S I and Fortov V E 2011 *Contrib. Plasma Phys.* **51** 367–74
[57] Mayer A E and Mayer P N 2015 *J. Appl. Phys.* **118** 035903